











**Compressive effects in melting of palladium thin films studied by ultrafast x-ray diffraction**

Ana F. Suzana <sup>1,\*</sup>, Robert Koch,<sup>1</sup> Longlong Wu <sup>1</sup>, Tadesse A. Assefa <sup>1</sup>, Sungwon Kim,<sup>2</sup> Sungwook Choi <sup>2</sup>, Heemin Lee <sup>3</sup>, Sunam Kim <sup>4</sup>, Jae Hyuk Lee <sup>4</sup>, Sang-Youn Park,<sup>4</sup> Daewoong Nam,<sup>4</sup> Sangsoo Kim <sup>4</sup>, Hyojung Hyun <sup>4</sup>, Kyung Sook Kim,<sup>4</sup> Gwen Wright,<sup>5</sup> Emil S. Bozin,<sup>1</sup> Changyong Song,<sup>3</sup> Hyunjung Kim,<sup>2</sup> Simon J. L. Billinge <sup>1,6</sup> and Ian K. Robinson<sup>1,7,†</sup>

<sup>1</sup>Condensed Matter Physics and Materials Science Department, Brookhaven National Laboratory, Upton, New York 11973, USA

<sup>2</sup>Department of Physics, Sogang University, Seoul 04107, Korea

<sup>3</sup>Department of Physics and POSTECH Photon Science Center, Pohang University of Science and Technology, Pohang 37673, Korea

<sup>4</sup>Pohang Accelerator Laboratory, Pohang, Gyeongbuk 37673, Korea

<sup>5</sup>Center for Functional Nanomaterials, Brookhaven National Laboratory, Upton, New York 11973, USA

<sup>6</sup>Department of Applied Physics and Applied Mathematics, Columbia University, New York, New York 10027, USA

<sup>7</sup>London Centre for Nanotechnology, University College London, London WC1E 6BT, United Kingdom



(Received 9 November 2022; accepted 24 May 2023; published 12 June 2023)

With the advent of x-ray free electron lasers (XFELs), ultrafast laser excitation leading to nonequilibrium states has become an important way to investigate thermal processes. Here, we use ultrafast x-ray diffraction in an XFEL pump-probe experiment to examine the lattice dynamics of 300 nm polycrystalline palladium (Pd) thin films. In our experiment, at higher laser fluence levels, we directly observe a compression effect launched from the surface skin layer heated by the optical pulse which propagates across the film over the first tens of picoseconds. After that, a lattice expansion becomes dominant, followed by a quasi-steady state lasting into the nanosecond timescale. For the lowest fluence, the compression component is not detected, indicating that the dynamics is highly dependent on the laser power. Our results shed light on the dynamics behind ultrafast processes in metallic Pd, and they can be extended to different crystalline structures.

DOI: [10.1103/PhysRevB.107.214303](https://doi.org/10.1103/PhysRevB.107.214303)

**I. INTRODUCTION**

With the increasing availability of femtosecond x-ray pulses at x-ray free electron laser (XFEL) facilities to probe transient structures, it has become possible to investigate laser-excited materials in nonequilibrium transient states. Both the original and transient states can be investigated using the pump-probe methodology. In particular, ultrafast x-ray diffraction (XRD) can probe structural phase transformations [1], transient melting states in nanocrystals [2], and thin films [3], revealing information about their dynamics. Likewise, the dynamics of the laser-driven nonequilibrium thermal processes leading to expansion/compression of the crystalline structure have been investigated using XFEL XRD [4,5].

The two-temperature model (TTM) has been successfully applied to explain the ultrafast electronic relaxation of various metallic systems [6,7], taking into account the coupling between different temperature carriers under these far from equilibrium conditions. In an ultrafast

pump-probe experiment, a femtosecond exciting laser pulse transfers its energy to the electrons, generating the so-called hot electrons. These electrons then travel through the sample, and couple with the lattice via electron-phonon coupling until the temperature between them equilibrates after a few picoseconds [6]. There is a shape-dependent acoustic response to the pump, with propagation of phonons within the solid, causing the oscillation of the structure. The results reporting this type of experiment are mostly for nanoparticles and thin films. Several investigations have studied the changes in the crystalline structure after the laser reaches the sample. Gan *et al.* [8] studied the ultrafast melting of Au thin films with varying thicknesses using a 100 fs, 800 nm, 180 mJ/cm<sup>2</sup> laser pump in a theoretical approach including the TTM and a molecular dynamics (MD) model. For all the thicknesses investigated (125–500 nm), the authors reported the growth of a melting front moving away from the impinging laser spot on the front surface, while solid Au remained all the way from the liquid-solid interface to the back of the sample. The melting front grows in the first tens of picoseconds (ps), followed by a recrystallization process starting at 80 ps for the 250 nm thickness film. However, the authors did not explore the effect of the electron blast force on the lattice constant of the solid part of the films. Sokolowski-Tinten [9] and coauthors studied the ultrafast laser irradiation of a 170 nm Ge thin film by measuring rocking curves of the (111) Bragg peak with varying time delays. In the collected rocking curves, a new peak appears at higher momentum transfer,  $Q$ , at first, indicating

\*asuzana@anl.gov

†irobinson@bnl.gov

compression, followed by the appearance of a new peak in the opposite direction (expansion) at later time delays. This was interpreted as a compressive strain caused by the near surface layer of pressurized molten Ge, followed by the coexistence of both compressed and expanded crystalline Ge, and finally in a late stage just the low- $Q$  peak is seen, indicating relaxation and the presence of a thermally expanded crystalline structure. The initial pressure is the highest in the molten surface layer, as the laser energy is mostly absorbed on the volume 40–50 nm underneath the surface, which explains the compressive strain launched from the surface. The authors also estimated the melt-front velocity to be 850 m/s, indicating the presence of superheated atoms at the solid-liquid interface.

The classical melting process has been extensively investigated, and it is believed to be initiated at defects of materials such as stacking faults, point defects, and surfaces and internal interfaces, such as grain boundaries in polycrystalline materials [10] at temperatures below the bulk melting transition. As the temperature increases and gets closer to the melting temperature, the regions close to the grain boundaries go to a disordered liquidlike layer in a process called grain boundary premelting [11]. Classical surface melting theory predicts that a liquid film starts to form at the solid-vapor interface at a given temperature and, depending on the free energy of the system, the temperature can be lowered (premelting) converting the outer layer to liquid [12]. This mechanism can considerably influence the bulk properties of a material as it enhances the grain boundary diffusivity and mobility [13]. Despite its importance, grain boundary premelting is still not fully understood due to the lack of experimental tools sensitive to the presence of grain boundaries. In our earlier experiment reporting the melting mechanism in Au polycrystalline thin films [3], we were able to identify an inhomogeneous melting mechanism due to the splitting of the (111) Bragg peak. We attributed this to a melting band originating from the grain boundaries and propagating into the grains.

Here we report an ultrafast XFEL XRD experiment where we probe the lattice dynamics in polycrystalline 300 nm Pd thin films driven by an 800 nm wavelength femtosecond laser pulse. Our experiment was performed at the Pohang Accelerator Laboratory X-Ray Free Electron Laser Facility (PAL XFEL), and it shows an interesting sequence of events with notable differences from the previous experiments on Au. We attribute these differences to the higher grain boundary density of Pd and also to differences in the electronic contributions to the melting pathway.

## II. EXPERIMENT

### A. Preparation of Pd thin films

Palladium films with a thickness of 300 nm were prepared by electron beam evaporation on silicon nitride ( $\text{Si}_3\text{N}_4$ ) window membranes at the Center for Functional Nanomaterials (CFN) at Brookhaven National Laboratory (BNL). The windows are 50 nm thick, arranged in  $23 \times 23$  arrays on silicon wafers,  $500 \mu\text{m} \times 500 \mu\text{m}$ . The equipment was left pumping overnight, and the deposition was done at lower pressures ( $\sim 10^{-7}$  Torr) to avoid the presence of impurities on the thin films.

### B. Pump-probe experiment

XFEL pump-probe experiments were carried out at Pohang Accelerator Laboratory X-Ray Free Electron Laser (PAL XFEL). The pump is composed of an 800 nm femtosecond laser system delivering fluences in the range of 250 – 800  $\text{mJ}/\text{cm}^2$  in the case of our experiment, with a pulse duration of 50 fs. The 800 nm wavelength laser has been chosen because, despite the fact that the reflectivity of Pd is significant at this wavelength, the absorption is still strong. The laser focal spot size was estimated to be 240  $\mu\text{m}$  full width at half maximum (FWHM) and the fluence was calibrated with a power meter. A collinear geometry was used with the laser incidence about  $10^\circ$  inclined to the x-ray beam. The silicon nitride membranes were mounted in a specially designed sample holder perpendicular to the beam in a Debye-Scherrer geometry as described elsewhere [3]. The change in the crystalline structure was probed using a Rayonix MX225 detector ( $5760 \times 5760$  pixels of  $39 \times 39 \mu\text{m}^2$ ),  $2 \times 2$  binned and placed 100 mm behind the sample to record the diffraction pattern in single shots from the XFEL running at 10 or 30 Hz. The crystalline structure of the Pd thin films was investigated before and after the laser irradiation. PAL XFEL was run in a self-seeded mode with no monochromator generating 9.7 keV x-ray photons in the undulator fundamental. The bandwidth of the self-seeded FEL beam was 0.35 eV (FWHM), the pulse duration was  $< 40$  fs, and the photon flux was 550  $\mu\text{J}$ . No filters were used for the data shown here. The XFEL x-ray beam was focused to approximately 10  $\mu\text{m}$  at the sample position, measuring the diffraction pattern as a function of pump-probe time delay. The sample membrane arrays were mounted on a motorized scanner synchronized to the XFEL beam, which visited each window of the membrane array for four successive shots before moving to the next window. Scans of the pump-probe delay, running from negative to positive, were synchronized with the movement between windows, so there were four repeated measurements at the same delay on each membrane.

### C. XRD data analysis and peak function fitting

The software PYFAI [14] was used to refine the sample to detector distance, the position of the direct beam, detector angles, and wavelength, using a “self-calibration” procedure on the negative time delay Pd diffraction pattern. Then the azimuthal integration was done for the measured diffraction patterns for negative and positive time delays. The next step was to fit the data using least-squares minimization curve fitting using the LMFIT package in PYTHON. After laser excitation, the diffraction profile was observed to split into as many as three separate peaks, sometimes overlapping, similar to what was seen in Ge [9]. The peak closest to the starting position (seen at negative time delays) was attributed to the unmelted crystal. Thermal expansion is expected to move the peaks to lower  $Q$ , while pressure is expected to move the peaks to higher  $Q$ , so the peak on the low- $Q$  side was attributed to lattice expansion, by analogy with the Au thin-film experiments [3], while that on the high- $Q$  side was attributed to a region of the sample under compression [9].

After testing the classical peak line shapes (Gaussian, Lorentzian, Voigt, and pseudo-Voigt), the function that gave

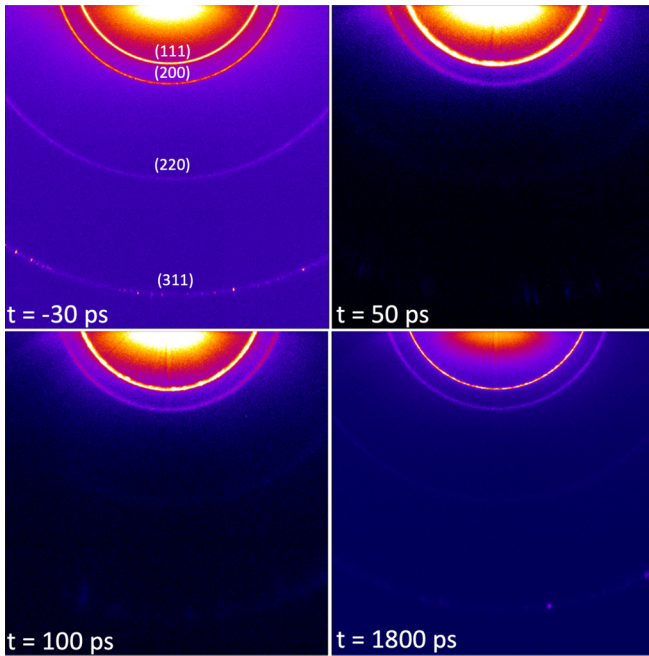


FIG. 1. 2D diffraction patterns at different pump-probe time delays for the laser fluence  $800 \text{ mJ/cm}^2$ . A broadness of the diffracted radiation is clearly seen for time delays of 50 and 100 ps, indicating changes in the lattice spacing  $d$ . The (111), (200), (220), and (311) reflections are labeled in the first plot (top left).

the best fitting was the pseudo-Voigt. A model was then built with one or more pseudo-Voigt functions (see below) and a linear background. After studying the quality and stability of the fitting model, the model parameters were then constrained differently for different regimes of the measurements:

*For the  $800 \text{ mJ/cm}^2$  fluence.* The crystalline peak was fitted by constraining the full width at half maximum (FWHM) to the value optimized by the negative time delays for the time delay range 1–50 ps. The FWHM was allowed to vary for the time delay range of 60–400 ps. The amplitude and center of the peaks were allowed to vary for all the time delays for all, crystalline, compressive, and expansive peaks.

*For the  $250 \text{ mJ/cm}^2$  fluence.* The FWHM, amplitude, and center were not constrained for the crystalline and expansive peaks.

### III. RESULTS AND DISCUSSION

The ultrafast XFEL XRD experiment was carried out in a transmission Debye-Scherrer geometry (details in the Experiment section). The 300 nm Pd thin films were illuminated by an 800 nm wavelength laser with varying fluences and pump-probe time delays. We measured the response of the crystalline thin film for time delays as large as 2.7 ns and observed several interesting physical phenomena. Figure 1 shows the two-dimensional (2D) diffraction patterns before laser incidence ( $-30 \text{ ps}$ ), and after, with varying positive time delays (50, 100, and 1800 ps) for the laser fluence of  $800 \text{ mJ/cm}^2$ . The (111), (200), (220), and (311) reflections are indicated for the negative time delay. For positive time delays, there is a visible broadening/shift of the diffraction

peaks, although it is not clear from these plots if it is a compression (broadening/shift toward higher angles), or expansion (broadening/shift toward smaller angles) effect. To check these effects, we performed line shape fitting on integrated 2D diffraction patterns, and Fig. 2 shows the resultant one-dimensional (1D) plots for time delays (a) up to 12 ps, (b) up to 38 ps, (c) 50 ps, (d) up to 400 ps, and (e) up to 2700 ps for the laser fluence of  $800 \text{ mJ/cm}^2$ .

In an optical/x-ray pump-probe experiment, the x-ray probe penetration depth is significantly larger than the one coming from the optical radiation. This is often referred to as the spatial overlap problem. Particularly for metals, the optical absorption depth is shorter at higher fluences due to nonlinear contributions to the absorption [15]. Consequently, only a thin layer (electromagnetic skin depth) on the surface will be directly affected by the optical pulse. On the other hand, the penetration depth of the x rays is much larger, usually a few microns, probing the whole Pd layer thickness (300 nm) in the case of our experiment. One can calculate the skin depth of the laser into the film using the following equation [16],

$$P = \frac{\lambda_{\text{laser}}}{4\pi \text{Im}(N)}, \quad (1)$$

where  $P$  is the penetration skin depth,  $\lambda$  is the laser wavelength, and  $\text{Im}(N)$  is the imaginary part of the complex conductivity. Considering the 800 nm laser used in our experiment and  $\text{Im}(N) = 5.438$  [17],  $P = 11.7 \text{ nm}$ . Therefore, only a small fraction of the diffracted intensity will correspond to the sample volume directly affected by the laser. It is well known from the TTM that the laser only interacts with electrons in the sample, which then have to couple to the crystal lattice before any changes can be seen in the atom positions with the x-ray probe. Regarding the aspect of delivered versus deposited energy, we can calculate the energy fraction absorbed for the linear regime, knowing the reflectivity at 800 nm. This would follow the relationship  $A = 1 - R - T$ , where  $A$  is the absorptivity,  $R$  is the reflectivity, and  $T$  is the transmission into the sample, which is assumed to be absorbed. But we do not have fluence-dependent reflectivity data to provide information about the nonlinear regime.

Given that the optical energy is deposited in a skin of only  $\sim 12 \text{ nm}$  on the 300 nm thin-film surface and assuming the TTM, we need to estimate how the distribution of generated hot electrons evolves before coupling to the lattice and heating it. We expect thermal layering in the sample before it reaches a quasiequilibrium. We can interpret the main effects in the whole crystalline Pd sample by analyzing the diffraction patterns collected over different time delays and fluences. In fact, we can see the formation of a compressive wave for higher fluences as a peak on the high- $Q$  side of the Pd (111) crystal peak, whose magnitude is highly dependent on the fluence. Figure S1 of the Supplemental Material [18] shows the plot for different fluences for time delay = 50 ps. The intensity was normalized by dividing its values by the maximum. This peak was not seen at  $250 \text{ mJ/cm}^2$  fluence, nor was it seen at any fluence in 300 nm Au films studied in the same way previously [3]. Compression peaks have been previously reported for Ge [9], Cu [4], and Au [5] thin films. As we discuss below, compression can occur when only the outer fraction of the sample is heated by the laser-driven hot electrons causing



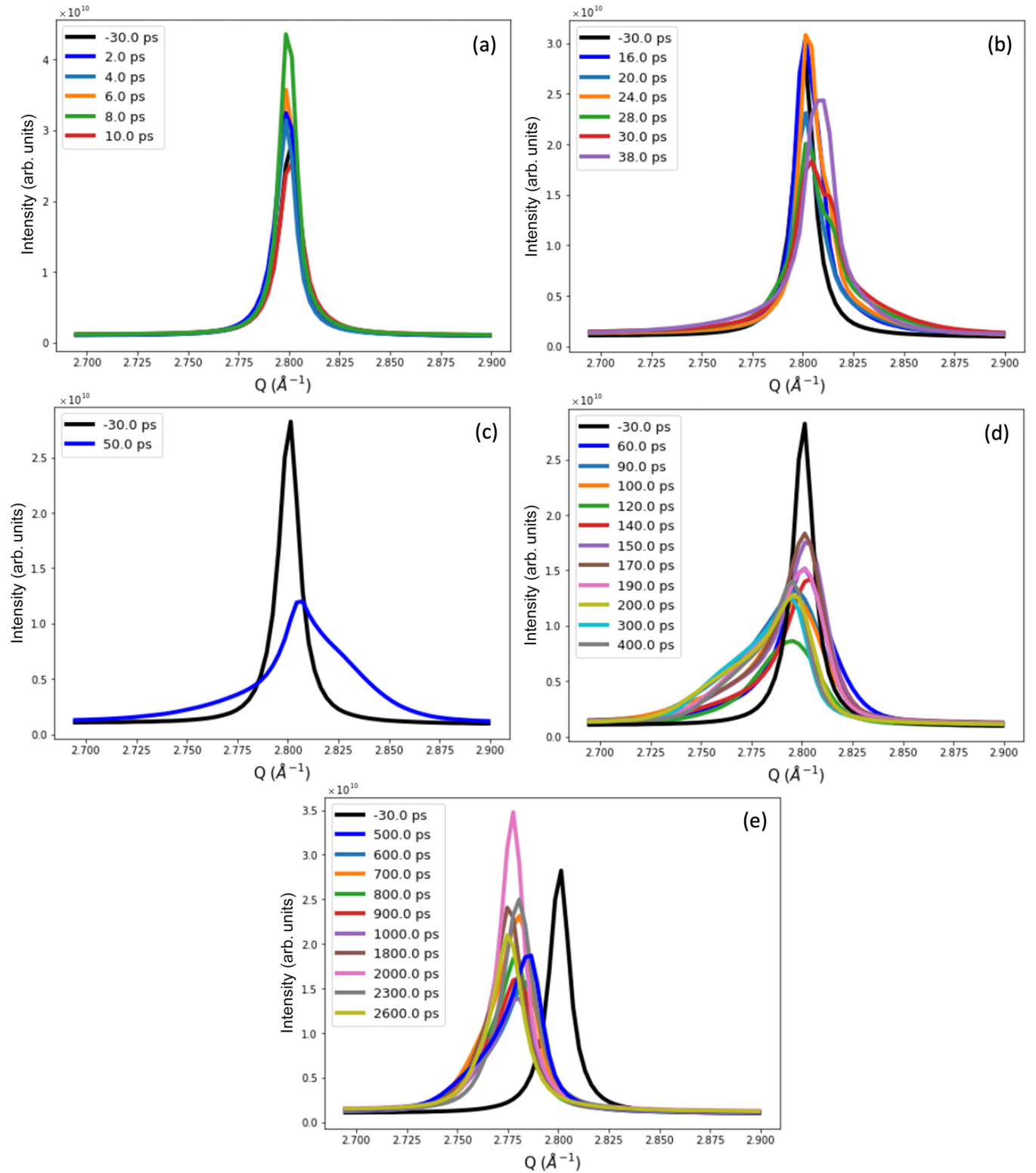


FIG. 2. XRD profiles of the (111) reflection using a laser fluence of  $800 \text{ mJ/cm}^2$  at different time delays: (a) up to 10 ps, (b) up to 38 ps, (c) 50 ps, (d) up to 400 ps, and (e) up to 2600 ps. The negative time delay corresponding to  $-30$  ps (before the laser reaches the sample) is shown in all plots.

it to expand and apply pressure on the remainder of the film. The longitudinal velocity of the acoustic wave  $v_l$  in Pd is  $3070 \text{ m s}^{-1}$ . For a 300 nm Pd film, the estimated time for longitudinal acoustic phonons to completely cross the

sample is approximately 98 ps. The period of the expected film vibration  $T$  is therefore given by  $T = 2L/v_l$ , where  $L$  is the thickness of the thin film, estimated to be 195 ps. The compression regime in 300 nm Pd films lasts only until  $\sim 50$  ps

before it reverses; this is only about half the transit time of acoustic waves traveling at the speed of sound, suggesting that the electronic-driven expansion pulse fills about half the sample thickness at this time. These results are different from the results reported by Assefa *et al.* [3] where the peak only shifted to lower  $Q$  in the integrated diffraction pattern.

For the  $800 \text{ mJ/cm}^2$  fluence, we distinguish five distinct time regimes altogether, whose plots are shown for the Pd (111) peak in Figs. 2(a)–2(e). The first regime includes time delays up to 14 ps [Fig. 2(a)], where the crystalline structure is preserved, with no apparent broadening or appearance of any new peak. The second regime [Fig. 2(b)] comprises time delays in the range of 15–38 ps, where there is little observable expansion (peak shift to the low- $Q$  side) but there is a pronounced contribution of compressive strain (peak shift to the high- $Q$  side). Figure 2(c) shows the maximum compression seen, reaching its maximum value of  $Q$  for time delay = 50 ps, which we consider to be the third regime in our analysis. Several shots were verified, and this behavior was seen for most of them. The fourth regime includes time delays in the range of 60–400 ps, where the contribution of the low- $Q$  side peak, associated with higher temperature, becomes more pronounced and it turns into the dominant contribution for time delays > 90 ps [Fig. 2(d)] whereas the contribution of the compression part becomes much less distinct. Finally, the last regime involves time delays in the range 500–2700 ps, where the initial crystalline peak is completely suppressed, moving to a lower- $Q$  region, appearing to be a steady state, presumably composed of thermally expanded material [Fig. 2(e)]. Qualitatively similar behavior is seen for other laser fluences used in our experiment ( $400 - 700 \text{ mJ/cm}^2$ ). The time delay of the maximum  $Q$  compressive peak varies slightly in the range of 40–50 ps. Especially for the  $800 \text{ mJ/cm}^2$  laser fluence, the signal of the compressive peak is rather broad, indicating the coexistence of multiple lattice constants. This suggests a heterogeneous strain buildup implying a distribution of pressures in the compression wave. This is the dominant feature in the diffraction profile for the earliest time delays.

When we then fitted the data shown in Fig. 2, the peak center, FWHM, and amplitude were well described by a pseudo-Voigt peak function (see details in the Experiment section above). Figure 3 displays one example of the fitting for each regime described above. The first regime [Fig. 3(a)] was fitted using a single component corresponding to the solid diffraction crystalline peak, with the center of the Bragg peak moving slightly to a higher  $Q$  (compression regime,  $Q = 2.8006, 2.7987, 2.7995, \text{ and } 2.8007 \text{ \AA}^{-1}$  for time delays –30, 4, 8, and 10 ps, respectively). After that, for time delays in the second regime, the initial solid diffraction crystalline peak is still there, and a second peak corresponding to compression becomes apparent [Fig. 3(b)]. The best fit was taken using three components: one corresponding to the crystalline peak and two components representing the compressive part. We interpret the need to have two compressive components as reflecting the presence of a pressure distribution associated with the compression. At this point, comprising time delays of 40–50 ps, there is the first appearance of an expansion component on the low- $Q$  side, so the 40 and 50 ps data were fitted using three components [expansive, crystalline,

and compressive peaks in Fig. 3(c)]. The expansion peak becomes visible from time delays greater than 50 ps; we can notice that its fitted position does not correspond to the lattice parameter of Pd at its melting point, which is shown as the black line on the left side of Fig. 3(c). As previously seen for Au films, we attribute this to a residual pressure in the film, calculated to be 2.3 GPa, following the approach described by Assefa *et al.* [3]. The fourth regime (60–400 ps) was best fitted with one crystalline peak and one expansive peak [Fig. 3(d)]. The last regime (500–2700 ps) was fitted with two expansive components.

Figure 4(a) shows the integrated plot for varying time delays for the lowest fluence used in our experiment,  $250 \text{ mJ/cm}^2$ . The remarkable difference between these plots and the data collected at the higher fluences is the absence of any clear compressive component in the diffraction patterns. For fitting these data, we used two components, one crystalline, and one expansive. Figure 4(b) shows one example of the fitting for  $t = 300$  ps, and Figs. 4(c) and 4(d) show the FWHM and peak center position, respectively, resulting from the fitting of both peaks. The FWHM of the expansive peak decreases over time. This is the same behavior found in Au thin films [3], which were interpreted in terms of a melting front forming a block of material at the melting point, which becomes bigger as a function of time delay, with the range shown. The peak center position for both peaks show damped oscillations coming from the traveling of the acoustic waves in the crystalline structure. The estimated period of the oscillations is around 190 ps, in good agreement with the expected value discussed above.

We now discuss our observation of the compressive component for the higher fluence in Pd thin films, which was not seen in Au. This can be attributed to higher electron temperatures for larger fluences, leading to a smaller mean free path according to the universal curve [19]. We can estimate the electron temperature (energy) for Pd by considering that all the pump energy is picked up by the approximately two free electrons per atom within the skin depth of the laser (12 nm). This gives 62 eV (719 000 K) per electron at the highest fluence of  $800 \text{ mJ/cm}^2$  and 20 eV (232 000 K) at  $250 \text{ mJ/cm}^2$ . The formula proposed by Seah and Dench [20] to calculate the inelastic mean free path gives a mean free path of 0.46 nm for the highest fluence ( $800 \text{ mJ/cm}^2$ ) and 0.61 nm for  $250 \text{ mJ/cm}^2$ . As the electrons scatter in the metal, they lose energy and their mean free path becomes rapidly longer according to the universal curve [19], reaching 100 nm once the energy has dropped to 1 eV, but the strong trend with electron energy suggests that the electrons from the highest fluence will fill a depth ten times smaller than the lowest. While we do not have realistic estimates of the effective electron penetration length scale, we know this distribution is established on the femtosecond timescale before the coupling to the lattice takes place on the 1–2 ps timescale. The compression effects seen at high fluence can be attributed to electron-lattice heating of only the top fraction of the sample thickness, followed by acoustic propagation of a pressure wave into the back of the sample. The absence of a compression signal at low fluence would then correspond to an electron distribution filling a much bigger fraction of the sample.

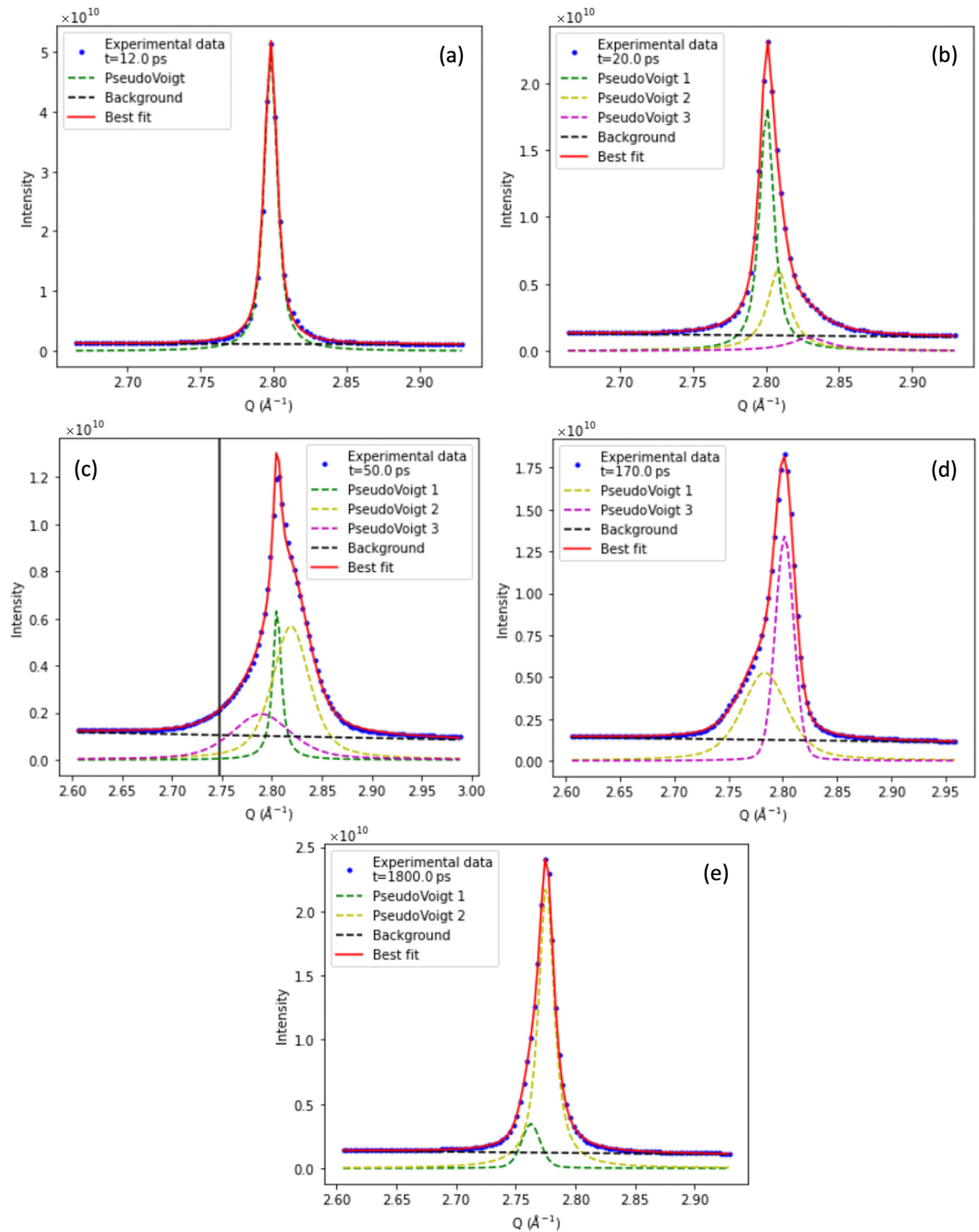


FIG. 3. Examples of the fittings using the pseudo-Voigt function for the laser fluence of  $800 \text{ mJ/cm}^2$  and time delays (a) 12, (b) 20, (c) 50, (d) 170, and (e) 1800 ps. The linear background function used in the fitting procedure is shown in the plots.

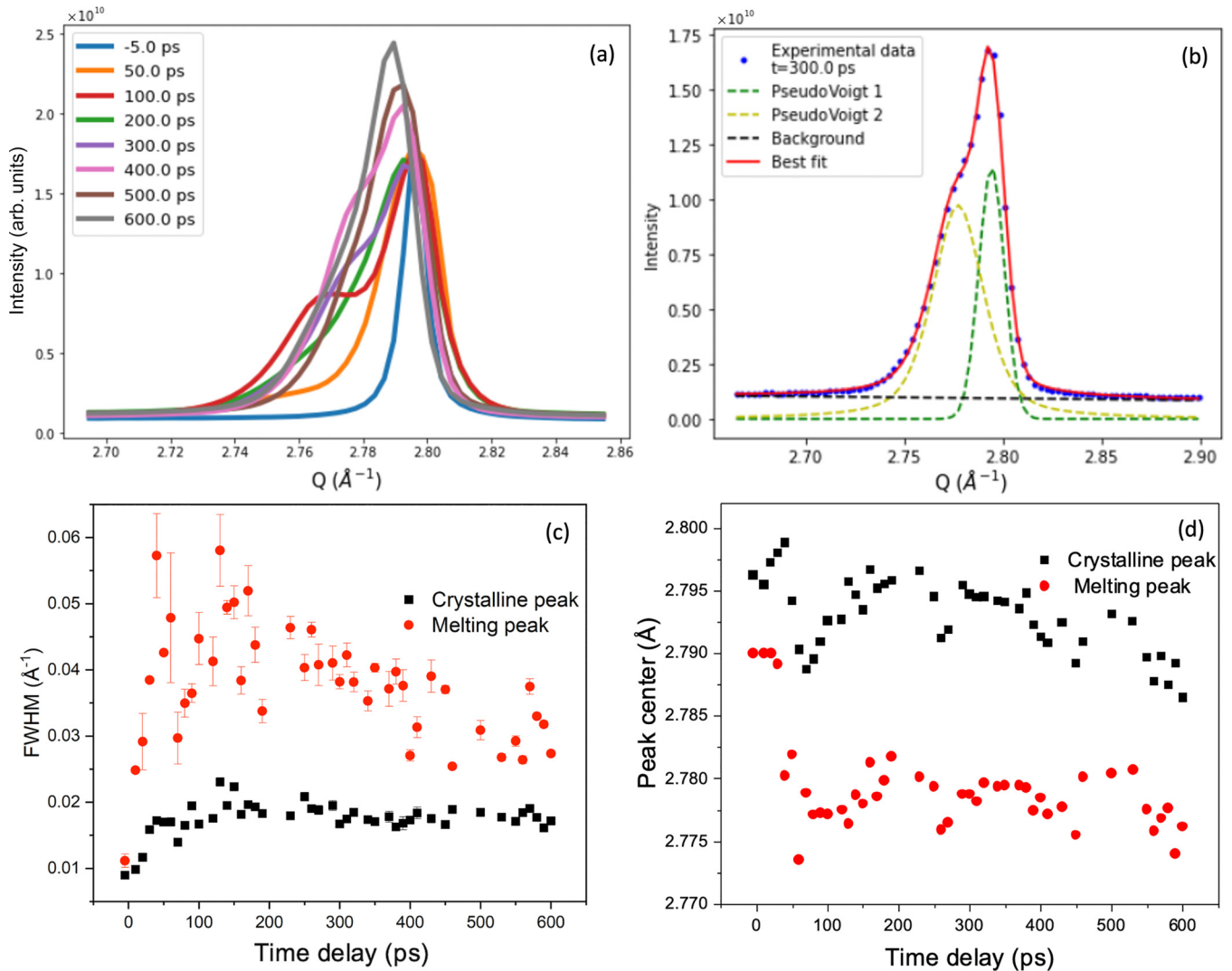


FIG. 4. (a) XRD patterns of the (111) reflection for the laser fluence of  $250 \text{ mJ/cm}^2$  at different time delays. (b) Pseudo-Voigt function peak fitting using a crystalline and an expansive component for  $t = 300 \text{ ps}$ . (c) FWHM and (d) peak center position coming from the fitting for both components.

The behavior seen for Au thin films at all fluence levels is similar to Pd at  $250 \text{ mJ/cm}^2$ , where the hot electrons travel the whole film thickness. This behavior can also be attributed to the different electron mean free paths for the two metals: the electron mean free path is larger for Au, as reported earlier [21,22]. This is also supported by the calculation above for Au, considering one valence electron: the electron mean free path for the  $800 \text{ mJ/cm}^2$  fluence is  $0.57 \text{ nm}$ , compared with  $0.46 \text{ nm}$  for Pd. The grain size calculated from the Scherrer formula [23] for the Pd (111) Bragg peak is  $58 \text{ nm}$  for our  $300 \text{ nm}$  Pd films, compared with  $163 \text{ nm}$  for the  $300 \text{ nm}$  Au thin films in our earlier work [3]. This implies a larger number of grains for Pd, hence an increase in the number of grain boundaries and a decrease in the electron mean free path due to an increase in electron scattering [18,24,25]. Experimental data have shown that there is an increase in the resistivity scaling up with the number of grain boundaries, induced by an increase of the electron scattering at the grain boundaries. Mayadas and Shatzkes [19] derived an expression for the electrical resistivity of wires with grain boundaries and found

that the grain boundaries act to reduce the mean free path of the electrons.

Figure 5 displays the amplitude (area) derived from the fitting of (a) the crystalline peak, (b) the melting front peak, and (c) the average over all the time delays of the area of the expansion peak. Overall, the amplitude of the crystalline peak decreases over time up to a turning point of  $\sim 150 \text{ ps}$ , whereas the amplitude of the expansion peak increases up to this turning point, from where it shows a linearlike trend. We interpret this as liquid being formed (detailed discussion below) from the solid crystalline phase. There is no clear fluence dependence trend in the plots.

For the longest time delays up to  $2.7 \text{ ns}$ , data were recorded for fluences spanning the range  $400 - 800 \text{ mJ/cm}^2$ . For the laser fluence of  $250 \text{ mJ/cm}^2$  the longest time delay studied was  $600 \text{ ps}$ . For all fluences, the diffraction peak was seen to shift toward lower  $Q$  values and can be fitted with two components, showing that the temperature remained high. There was not enough time for significant thermal energy to be trans-

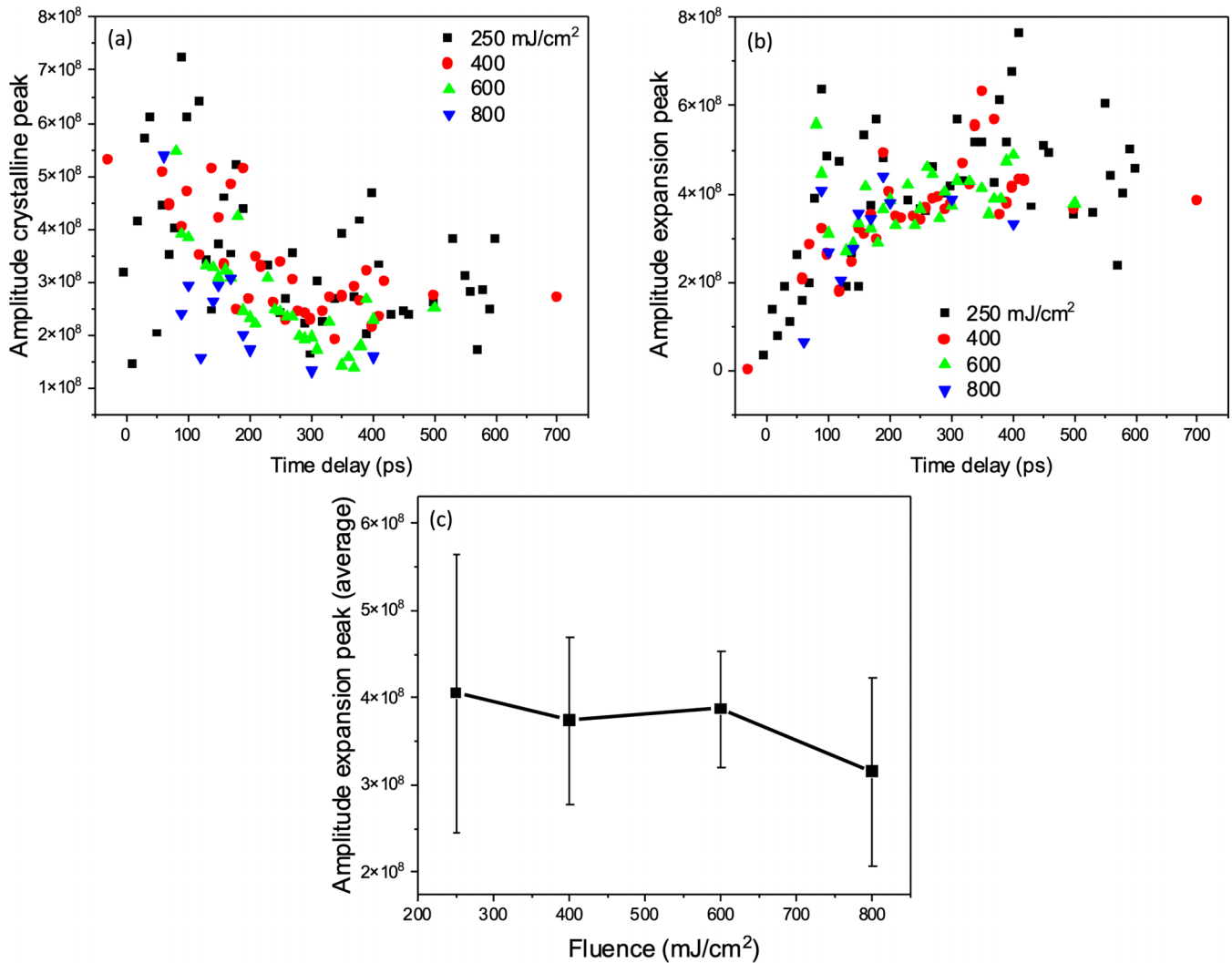


FIG. 5. Amplitude (area) derived from the fitting of (a) the crystalline peak, (b) the melting-front peak, and (c) average over all time delays of the amplitude of the expansion peak.

ferred to the environment by heat diffusion or any recovery of the hot crystal skin. The plots showing the diffraction pattern for  $t = -20$  ps and  $t = 2.7$  ns are shown in Fig. 6. The black line represents the  $Q$  value expected for the Pd crystal at the melting temperature (1828 K). The intensity was normalized by dividing the vertical axis by its maximum value. At the longest time delays, it appears that the sample reaches a steady state for all the fluences, with the Bragg peak shifted toward lower  $Q$  values (expanded crystalline structure) and complete disappearance of the solid diffraction peak. The shift is larger for the highest fluences, suggesting this long-time behavior is a classical heating effect. We fitted both time delays using pseudo-Voigt peak functions, and plotted the center versus the fluence, shown in Fig. 6 (bottom, right). There is a clear linear trend where the  $Q$  values decrease as the fluence increases, as expected as the higher fluences will deliver a higher energy density to the thin-film volume that absorbed the laser energy. The broadness of the (111) Bragg peak after 2.7 ns is consistently larger than the FWHM of the negative time delay, indicating the presence of multiple lattice constants. This could imply a temperature distribution, but it could also

be due to the building up of strain in the film coming from the relaxation process.

Having discussed all the time-delay regimes of the Pd (111) Bragg peak from the crystal, we now turn to the diffraction signature of the liquid phase, which contributes to the diffuse scattering in between the Bragg peaks. Positive and negative time delay scans were separately averaged together, and the negative time delay was subtracted from the positive in azimuth-integrated 1D diffraction plots. One example of the average 1D plot for negative and positive (100 ps) time delays is shown in Fig. 7. We then take the average intensity of the points in the region  $2.9 - 3.1 \text{ \AA}^{-1}$ , subtracting the background at a negative time delay. This region is safely away from the Bragg peaks, so it contains only the diffuse signal coming from the liquid phase. The liquid structure factor  $S(q)$  of Pd has its first and second peaks around  $2.8$  and  $5.2 \text{ \AA}^{-1}$  [26]. The liquid phase, if present, would present a broad peak around the chosen momentum transfer value, so the intensity should be a broad measure of the amount of liquid Pd. Figure 8 shows the result for time delays spanning 10–1000 ps for all the fluences studied, showing a roughly linear increase of the



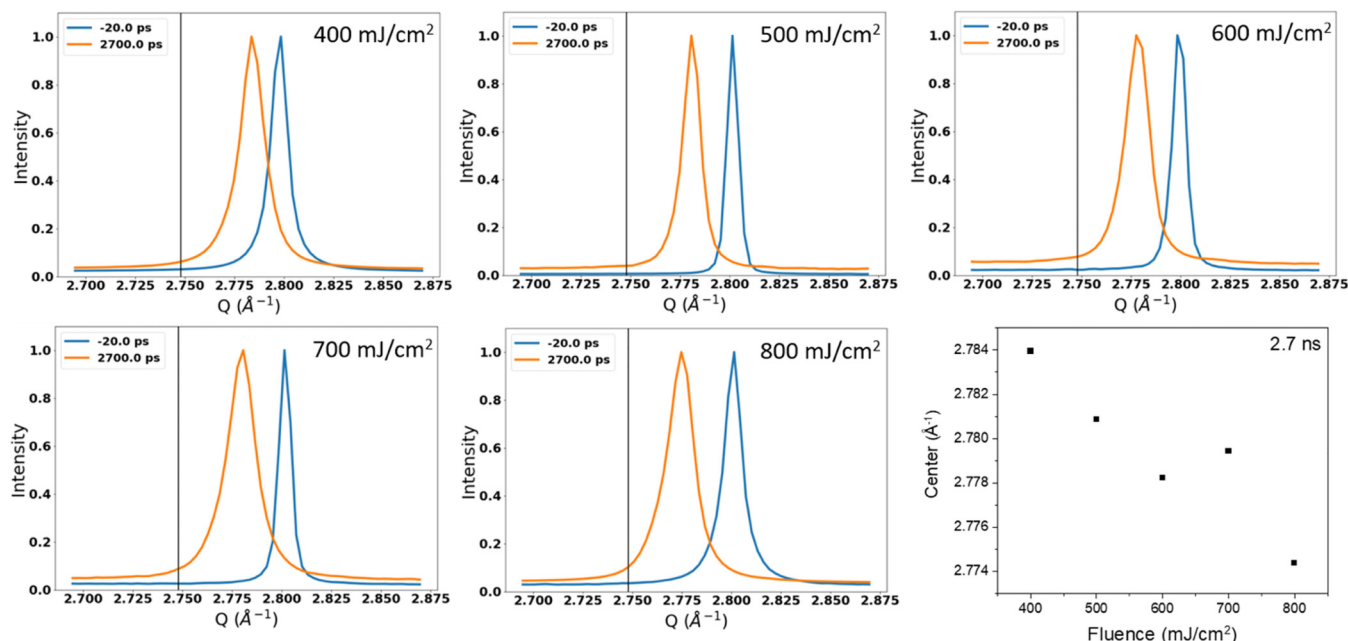


FIG. 6. Plot showing the XRD intensity versus momentum transfer,  $Q$ , for the (111) reflection before the laser shines on the sample ( $t = -20$  ps), and after, for the longest time delay investigated in our experiment ( $t = 2.7$  ns) for fluences ranging in the interval 400 – 800  $\text{mJ}/\text{cm}^2$ . The black line in the plots represents the  $Q$  value for Pd crystalline structure at the melting temperature (1828 K). The last plot (bottom, right) shows the center of the peak after 2.7 ns versus fluence.

liquid signal over time for time delays of 10–50 ps. For time delays in the range of 100–1000 ps, there is no visible trend in the signal. The error bars are large for these data because of the weak signal and large fluctuations of the XFEL source, which were not properly normalized. Attempts were made to filter the data for “bad shots,” but these were only partly effective.

The most noteworthy feature of the data is the absence of any strong fluence dependence of the diffuse scattering signal, either in the linear ramp regime (10–50 ps) or in the total

amount of liquid generated (100–1000 ps). We believe this is an effect of the inhomogeneity of the melting discussed above, whereby the depth penetrated by the laser-driven hot electron population becomes smaller at higher fluence. If we invoke the melt-front picture of heat entering the material at the grain boundaries of the thin film (where the hot electrons scatter) used to describe the melting of 300 nm Au films [3], we would expect higher fluences to create hotter electrons and so higher thermal spikes at the grain boundaries. This would drive the melt fronts faster into the grains and produce

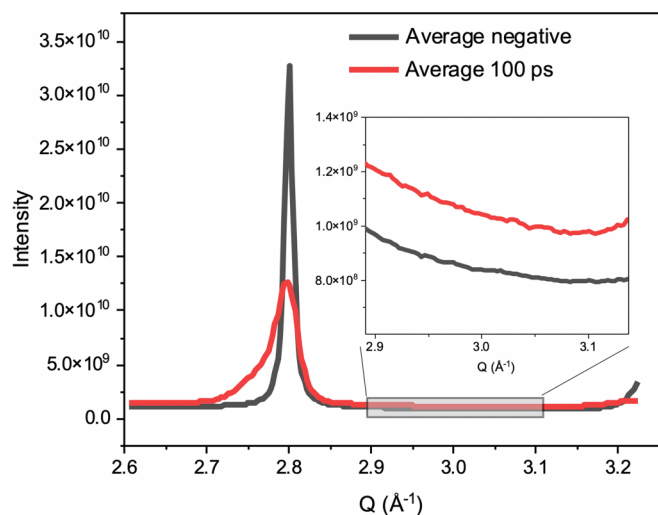


FIG. 7. 1D diffraction plots for the average of the negative and 100 ps time delays for 800  $\text{mJ}/\text{cm}^2$ . The background region corresponding to the liquid part of the structure is higher for positive time delays, as shown in the inset.

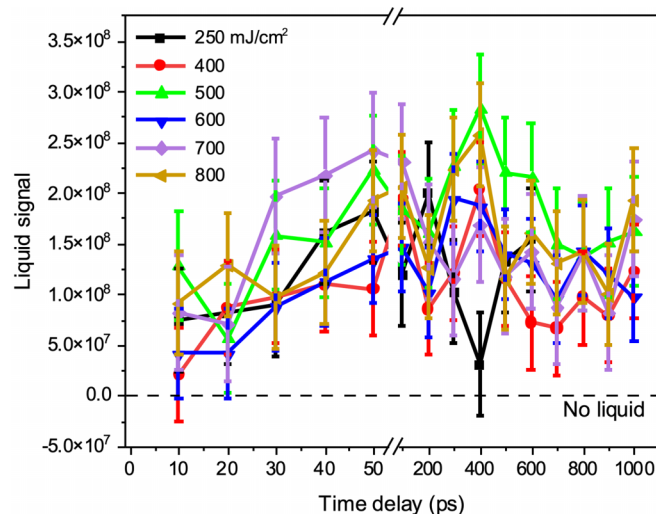


FIG. 8. Liquid signal extracted by subtracting negative from positive time delays, and then averaging the 2.9 – 3.1  $\text{\AA}^{-1}$   $Q$  region for time delays in the range 10–1000 ps for varying fluences.

liquid more rapidly. The combined effect of a smaller volume heated by the electrons and a faster melt front would give rise to roughly the same amount of liquid at each fluence level, which is what we observe. Excess heat in the outermost regions of the sample at the highest fluences might be expected to reach the boiling point of Pd, so some contribution from vaporization or ablation might also contribute to the apparent saturation of the amount of liquid at higher laser fluences. Indeed, microscope images were taken after the experiment, shown in Fig. S2 in the Supplemental Material [18], and show a corona of debris surrounding the location of the laser/x-ray shots.

We calculate the temperature rise of the entire film due to laser heating using the following formula [3],

$$\Delta T = \frac{\alpha F}{h\rho C_P}, \quad (2)$$

where  $\alpha = 0.52$  is the absorption coefficient of Pd,  $F$  is the incident laser fluence,  $h$  is the thickness of the thin film (300 nm),  $\rho$  is the density of Pd (12.023 g/cm<sup>3</sup>) and  $C_P$  is the Pd specific heat capacity (0.24 J/g K). For the laser fluences of 250, 400, 500, 600, 700, and 800 mJ/cm<sup>2</sup>, the calculated rise in temperature is 1502, 2403, 3004, 3604, 4203, and 4806 K, respectively, disregarding the contribution coming from latent heat. According to this approach, a fluence of about 305 mJ/cm<sup>2</sup> should be just sufficient to melt the film at  $T_M = 1828$  K, and a fluence of about 539 mJ/cm<sup>2</sup> would be just sufficient for vaporization to happen at  $T_B = 3236$  K. The amplitude of the expansion peak for 250 mJ/cm<sup>2</sup> laser fluence [Fig. 5(c)] is slightly larger than at higher fluence, indicating that the melting-front volume is larger for the lowest fluence. For the highest fluence studied (800 mJ/cm<sup>2</sup>), the average amplitude assumes the lowest value, suggesting that a larger portion of the thin film was vaporized.

Concerning the generation of laser-driven ballistic electrons in the dynamics described here, we indeed expect deeper penetration of nonthermal ballistic electrons excited by the laser which would travel further than the mean-free path. Unfortunately, there is no way of decoupling the effects of the ballistic and nonballistic electrons from the diffraction data.

#### IV. CONCLUSIONS

We were able to investigate the partial melting process of 300 nm polycrystalline Pd thin films for different fluences in a pump-probe XFEL XRD experiment. Five delay-time regimes were identified in the data for the highest fluences. A summary cartoon picture of the overall behavior of the films is shown in Fig. 9. For fluences spanning 400–800 mJ/cm<sup>2</sup>, there is the appearance of a compressive component in the diffraction data, indicating a behavior different from our earlier experiment done on Au thin films; it is argued that the compression comes from the limited penetration (at high fluence) of the laser-driven hot electrons, which heat the film from the top side and drive a pressure wave from the top toward the bottom of the film.

On the other hand, for the lowest fluence used in our experiment (250 mJ/cm<sup>2</sup>), the results are similar to those reported in our Au experiment, with the formation of an

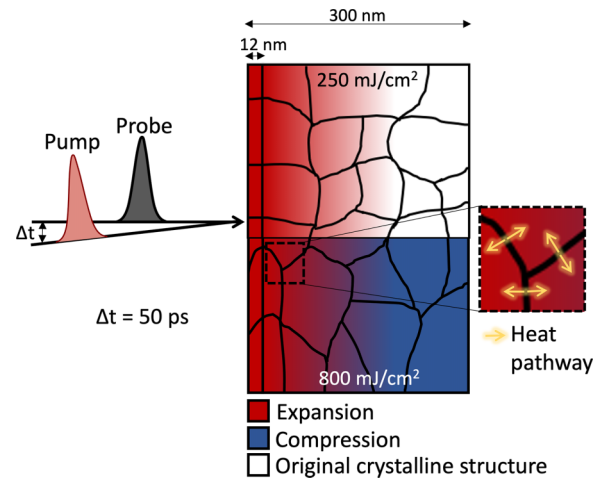


FIG. 9. Schematic representing a cross section of the Pd thin film at time delay = 50 ps; the  $\sim 12$  nm skin depth laser absorption layer is shown. There is expansion of the crystalline structure (represented by red) and for 250 mJ/cm<sup>2</sup> fluence (top), the crystalline structure is preserved for the second half of the film, whereas for 800 mJ/cm<sup>2</sup> (bottom) a compression wave (represented by blue) is launched into the rest of the film.

intermediate “expansion” diffraction peak, which we attribute to inhomogeneous melting starting at the grain boundaries and progressing toward the centers of the crystal grains. The release of latent heat in the resulting melt front traps a volume of crystal at its melting point while the melting takes place, and this gives rise to the “expansion” peak. The apparent discrepancy can be attributed to the different electron temperatures and mean free path for different fluences: the electrons created by the laser absorption do not travel through the whole film thickness for higher fluences, being scattered close to or at the grain boundaries. This picture is supported by the observation that the amount of liquid Pd, measured as the intensity diffuse scattering between the Bragg peaks, shows a linear rise up to 100 ps and then saturates with no strong fluence dependence. The lack of fluence dependence is attributed to the smaller volume of melting material being offset by the faster melt-front velocity at higher fluence.

We identify several timescales for the changes in the shape of the (111) diffraction peak. For these 300 nm thin films,  $\tau_c \sim 50$  ps appears to be the critical time, for the higher range of fluences studied (400–800 mJ/cm<sup>2</sup>). For  $t < \tau_c$ , there is increasing compression of the film, which reverses quite abruptly into expansion after  $\tau_c$ . The liquid signal increases up to  $t = \tau_c$  and remains roughly constant afterward. This critical time corresponds to acoustic propagation (at the speed of sound) over approximately half the film thickness. We therefore consider that the laser-driven hot electrons couple to the lattice in the outer half of the sample, transferring their energy to the lattice within the first few picoseconds, according to the TTM. This leads to inhomogeneous melting and partial vaporization in the outer layer and a transient acoustic wave which compresses the far side of the sample.

In principle, we could also pump metals with different photon energy than the one studied here (ultraviolet or soft

x rays, for instance). In this case, regarding the extreme ultraviolet soft x-ray range, the reflectivity, transmission, and absorptivity would be different. It is difficult to estimate these physical parameters, as they depend on the film thickness, the incidence angle, the incidence energy, etc. It would be interesting to repeat the experiment using a different laser photon energy, and probe the effect of this in the structure of the metal over time. Another aspect that is possible to explore further is the film thickness. We have chosen a 300 nm thin-film thickness for the current experiment because in our previous study [3], the diffraction signal of the 300 nm sample was the best. Taking into consideration the penetration depth of the laser ( $\sim 12$  nm), it would be interesting to perform the same experiment with thinner films. In this case, we expect a similar behavior as in the current experiment, with the timescale for the hot electrons to cross the film proportional to the thickness.

## ACKNOWLEDGMENTS

We acknowledge Luca Geliso and Ivan Vartanians for the helpful discussions about their parallel study of Pt thin films. Data analysis was supported by the DOE Office of Science by Brookhaven National Laboratory under Contract No. DESC0012704. The Center for Functional Nanomaterials, used for the fabrication of the thin films, is a U.S. DOE Office of Science User Facility operated for the DOE Office of Science by Brookhaven National Laboratory under Contract No. DESC0012704. Work performed at UCL was supported by EPSRC. Sungwon Kim, S.C., and H.K. acknowledge the support by the National Research Foundation of Korea (NRF-2021R1A3B1077076). This work was supported by the GSDC for data computing and the KREONET for network service provided by the KISTI.

- 
- [1] J. S. Wittenberg, T. A. Miller, E. Szilagy, K. Lutker, F. Quirin, W. Lu, H. Lemke, D. Zhu, M. Chollet, J. Robinson *et al.*, Real-time visualization of nanocrystal solid-solid transformation pathways, *Nano Lett.* **14**, 1995 (2014).
- [2] J. N. Clark, L. Beitra, G. Xiong, D. M. Fritz, H. T. Lemke, D. Zhu, M. Chollet, G. J. Williams, M. M. Messerschmidt, B. Abbey *et al.*, Imaging transient melting of a nanocrystal using an x-ray laser, *Proc. Natl. Acad. Sci. USA* **112**, 7444 (2015).
- [3] T. A. Assefa, Y. Cao, S. Banerjee, S. Kim, D. Kim, H. Lee, S. Kim, J. H. Lee, S. Park, I. Eom *et al.*, Ultrafast x-ray diffraction study of melt-front dynamics in polycrystalline thin films, *Sci. Adv.* **6** (2020).
- [4] D. Milathianaki, S. Boutet, G. J. Williams, A. Higginbotham, D. Ratner, A. E. Gleason, M. Messerschmidt, M. M. Seibert, D. C. Swift, P. Hering *et al.*, Femtosecond visualization of lattice dynamics in shock-compressed matter, *Science* **342**, 220 (2013).
- [5] N. J. Hartley, N. Ozaki, T. Matsuoka, B. Albertazzi, A. Faenov, Y. Fujimoto, H. Habara, M. Harmand, Y. Inubushi, T. Katayama *et al.*, Ultrafast observation of lattice dynamics in laser-irradiated gold foils, *Appl. Phys. Lett.* **110**, 071905 (2017).
- [6] I. Robinson, J. Clark, and R. Harder, Materials science in the time domain using Bragg coherent diffraction imaging, *J. Opt.* **18**, 054007 (2016).
- [7] J. K. Chen, D. Y. Tzou, and J. E. Beraun, A semiclassical two-temperature model for ultrafast laser heating, *Int. J. Heat Mass Transfer* **49**, 307 (2006).
- [8] Y. Gan, J. Shi, and S. Jiang, Atomic-level study of a thickness-dependent phase change in gold thin films heated by an ultrafast laser, *Appl. Opt.* **51**, 5946 (2012).
- [9] K. Sokolowski-Tinten, C. Blome, C. Dietrich, A. Tarasevitch, M. Horn von Hoegen, D. von der Linde, A. Cavalleri, J. Squier, and M. Kammler, Femtosecond X-Ray Measurement of Ultrafast Melting and Large Acoustic Transients, *Phys. Rev. Lett.* **87**, 225701 (2001).
- [10] A. M. Alsayed, M. F. Islam, J. Zhang, P. J. Collings, and A. G. Yodh, Premelting at defects within bulk colloidal crystals, *Science* **309**, 1207 (2005).
- [11] M. Torabi Rad, G. Boussinot, and M. Apel, Dynamics of grain boundary premelting, *Sci. Rep.* **10**, 21074 (2020).
- [12] J. G. Dash, Surfaces and surface films, *Proc. Natl. Acad. Sci. USA* **84**, 4690 (1987).
- [13] S. Divinski, M. Lohmann, C. Herzig, B. Straumal, B. Baretzky, and W. Gust, Grain-boundary melting phase transition in the Cu-Bi system, *Phys. Rev. B* **71**, 104104 (2005).
- [14] G. Ashiotis, A. Deschildre, Z. Nawaz, J. P. Wright, D. Karkoulis, F. E. Picca, and J. Kieffer, The fast azimuthal integration python library: PYFAI, *J. Appl. Crystallogr.* **48**, 510 (2015).
- [15] K. Sokolowski-Tinten, C. Blome, J. Blums, A. Cavalleri, C. Dietrich, A. Tarasevitch, and D. von der Linde, Ultrafast time-resolved x-ray diffraction, in *Science of Superstrong Field Interactions: Seventh International Symposium of the Graduate University for Advanced Studies on Science of Superstrong Field Interactions*, AIP Conf. Proc. No. 634 (AIP, Melville, NY, 2002), p. 11.
- [16] S. Orfanidis, *Electromagnetic Waves and Antennas* (Rutgers University, Piscataway, NJ, 2016).
- [17] K. J. Palm, J. B. Murray, T. C. Narayan, and J. N. Munday, Dynamic optical properties of metal hydrides, *ACS Photonics* **5**, 4677 (2018).
- [18] See Supplemental Material at <http://link.aps.org/supplemental/10.1103/PhysRevB.107.214303> for the diffraction plots at 50 ps at all the fluences studied and optical microscopy images taken after the experiment.
- [19] A. F. Mayadas and M. Shatzkes, Electrical-resistivity model for polycrystalline films: The case of arbitrary reflection at external surfaces, *Phys. Rev. B* **1**, 1382 (1970).
- [20] M. P. Seah and W. A. Dench, Quantitative electron spectroscopy of surfaces, *Surf. Interface Anal.* **1**, 2 (1979).
- [21] L. D. Bell, Evidence of Momentum Conservation at a Nonepitaxial Metal/Semiconductor Interface Using Ballistic Electron Emission Microscopy, *Phys. Rev. Lett.* **77**, 3893 (1996).
- [22] R. Ludeke and A. Bauer, Hot Electron Scattering Processes in Metal Films and at Metal-Semiconductor Interfaces, *Phys. Rev. Lett.* **71**, 1760 (1993).
- [23] A. L. Patterson, The Scherrer formula for x-ray particle size determination, *Phys. Rev.* **56**, 978 (1939).

- [24] D. Josell, S. H. Brongersma, and Z. Tokei, Size-Dependent Resistivity in Nanoscale Interconnects, *Annu. Rev. Mater. Res.* **39**, 231 (2009).
- [25] J. W. C. De Vries, Temperature and thickness dependence of the resistivity of thin polycrystalline aluminium, cobalt, nickel, palladium, silver and gold films, *Thin Solid Films* **167**, 25 (1988).
- [26] Z. J. Yang, L. Tang, T. Q. Wen, K. M. Ho, and C. Z. Wang, Effects of Si solute on the glass formation and atomic structure of Pd liquid, *J. Phys.: Condens. Matter* **31**, 135701 (2019).